Journal of Fluids and Structures (2000) **14,** 711–733
doi:10.1006/jfls.2000.0295, available online at http://www.idealibrary.com on IDEAL®

FINITE ELEMENT SURFACE MODEL FOR FLOW AROUND VERTICAL WALL ABUTMENTS

A. Molinas
Department of Civil Engineering, Colorado State University
Fort Collins, CO 80523, U.S.A.

AND

Y. I. Hafez
The Nile Research Institute, Water Research Center
Cairo, Egypt 13621

(Received 9 July 1999, and in final form 10 February 2000)

A two-dimensional finite element surface model is developed to determine velocities, depths, and turning angles around vertical wall abutments. The model solves the Reynolds-averaged turbulent flow equations along a horizontal plane passing through the average water surface. This approach is an improvement over the depth-averaged flow models where dispersion terms reflecting vertical effects are neglected. In the model, vertical gradient effects are accounted for through the use of power law for the vertical distribution of the longitudinal velocity; a similar treatment is applied to lateral turbulent shear stresses. The model is capable of computing the dynamic pressure distribution, which in turn is converted to water elevation values. The model, being two dimensional, is computationally efficient and practical to use. The numerical model was successfully verified using experimental data from vertical wall abutments and groins with protrusion ratios (ratio of protrusion length perpendicular to direction of flow to total channel width) of 0·1, 0·2 and 0·3. The results show the occurrence of a high intensity velocity zone close to the upstream abutment nose similar to those observed experimentally. The effects of roughness, depth, and energy slope on the intensity of flow field is investigated and an analytical expression is developed. Numerical experiments indicate that grain roughness affects flow field around the abutment nose by controlling the magnitude of the lateral velocity component and by controlling the lateral extent of the affected zone. Velocity amplification at the abutment nose is found to be mainly related to the protrusion ratio and to the friction factor, and can be up to 1·75 times the approach velocities for protrusion ratios of 0·3. For a protrusion ratio of 0·3, for a typical range of roughness values the increase in nose velocities due to friction factor alone was found to be up to 20 percent.

1. INTRODUCTION

In the hydraulic design of bridges, determination of flow distribution around abutments is an important aspect for the protection and safety assessment of structures. Bridge abutments constrict the oncoming flows and alter the approach flow patterns. As shown in Figure 1, the local increase in velocities and the resulting shear stresses cause scour around the abutments. In evaluating the scour potential around abutment foundations or in sizing the rip-rap material to be used for bank protection against scour, accurate estimation of the flow field is necessary.

In general, flow around hydraulic structures can be numerically simulated through the use of two-dimensional (2-D) or three-dimensional (3-D) turbulence models of varying complexities. Depending on the physical nature of flows and the zone of interest within the

0889–9746/00/070711 + 23 $35.00/0

flow domain, certain problems require the use of 3-D models (Ouillon & Dartus 1997; Mayerle *et al.* 1995; Hafez 1995). The 2-D models are appropriate for applications involving simplified flow regions (Bravo *et al.* 1996; Molls & Chaudhry 1995; Kimura & Hosoda 1997). Hafez (1995) explained that the non-linear k-ε turbulence models are necessary to determine the flow field in the cross-sectional plane of an open channel where corner effects are important. The use of simplified turbulence models has been discussed in great detail by Rodi (1993). The simplified models, if applicable, offer computational efficiency, require lower resolution input data, and contain much fewer calibration parameters. While Thangam & Speziale (1992) reported that large number of iterations were needed for the convergence of their standard k-ε turbulence model, the simplified constant eddy viscosity models such as those by Tan (1992), Benque *et al.* (1992), Kimura & Hosoda (1997) for solving engineering problems require much fewer iterations for convergence.

Past numerical investigations of water flow around abutments are based on several studies for flow around groins and dikes which can be visualized as very thin abutments. While the zone of interest in groins is mainly the recirculation zone behind the thin wall, in abutments the upstream nose and contracted regions are of primary concern. Knowledge of flow intensity in these regions is needed to design adequate protection against the scouring action of oncoming flows.

Tingsanchali & Maheswaran (1990) used a two-dimensional depth-averaged k-ε turbulence model for flow around groins. They incorporated a correction into their model to account for streamline curvature and applied a 3-D correction for the roughness effects. Tingsanchali & Maheswaran neglected the dispersion terms which appear in depth-averaged equations and which account for the vertical effects. They also assumed the pressure to have a hydrostatic distribution. Rodi (1993) stresses the importance of the dispersion terms in flows such as those around vertical wall abutments where there are strong vertical velocity gradients. Mayerle *et al.* (1995), analyzing their results from six turbulence models for simulating flows near groins, attribute the discrepancy between computed three-dimensional flow patterns and experimental measurements to the assumption of hydrostatic pressure distribution whatever the turbulence model is.

Ouillon & Dartus (1997), investigating flow around groins, used a three-dimensional k-ε turbulence model along with both rigid-lid and three-dimensional free-surface versions of the model. The free surface model used the porosity method to track the free surface. Ouillon & Dartus' results showed that close to the nose region of the groin, which is the zone of interest for local scour computations, there was no discrepancy between the rigid-lid and free surface models; the difference in the flow field was at the zone of flow re-attachment (recirculation), away from the scour region. Ouillon & Dartus presented their results for the velocity field at two horizontal planes: one near the bed and the other near the free surface. These results show no significant difference in the flow pattern which would warrant the use of a complex three-dimensional model. Based on these findings, the rigid-lid assumption and a 2-D model along the free surface are justified for use in computing flow around vertical wall abutments.

Previous studies for dikes and groins mentioned above (Tingsanchali & Maheswaran 1990; Mayerle *et al.* 1995, Ouillon & Dartus 1997) focused on solving a particular flow problem and comparing simulation results with experimental measurements for a single protrusion ratio (ratio of protrusion length perpendicular to direction of flow, a, to total channel width, B, or a/B). Additionally, bed roughness, flow depth, flow intensity, and energy slope effects were not addressed which caused past calibration coefficients to only reflect a narrow range of applications. This study aims to investigate the effects of protrusion, bed roughness, flow depth, flow intensity, and energy slope on the flow field around vertical wall abutments for a wide range of flow conditions. For this purpose a

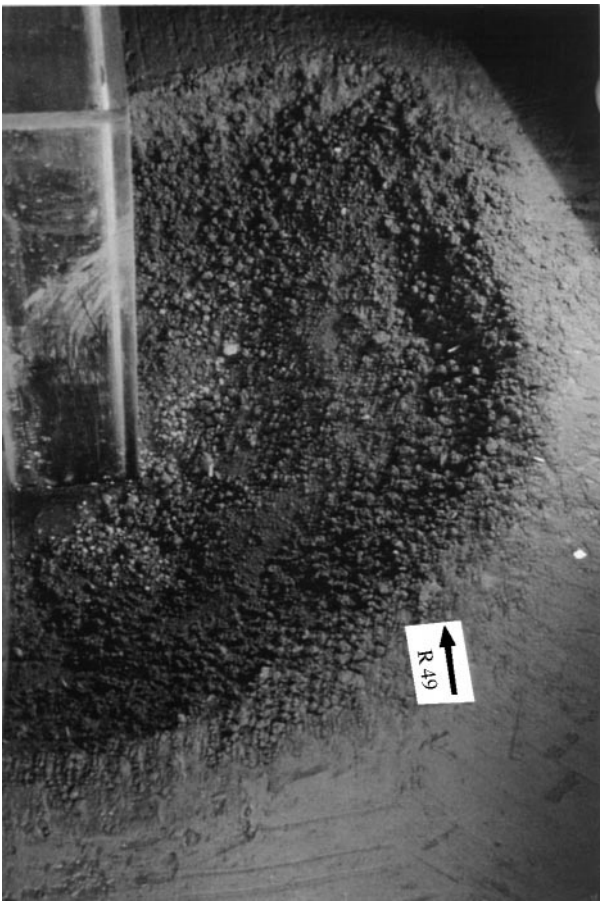

Figure 1. Local scour pattern around vertical wall abutments

two-dimensional hydrodynamic model was developed to determine the flow field around vertical wall abutments. The numerical model was successfully tested and verified against experimental data. Next, using this model, the effects of roughness on the flow field is investigated and an expression which relates maximum nose velocity amplification to friction and protrusion ratio is developed.

2. THE HYDRODYNAMIC MODEL

2.1. Governing Equations

A hydrodynamic model was developed for the prediction of the two-dimensional velocity, flow depth, and bed shear fields necessary for the calculation of bed scour around vertical wall abutments. The model is written in the Cartesian X-Y coordinates where the X-direction is in the main flow direction (longitudinal direction) and the Y-direction is in the lateral direction. The flow field in the horizontal plane is shown in Figure 2. The time-averaged Navier-Stokes equations (Reynolds-averaged equations) for the mean turbulent flow under steady and incompressible conditions constitute the hydrodynamic model. Along the water surface plane, the governing continuity and momentum equations in the X- and Y-directions are

$$\frac{\partial u}{\partial X} + \frac{\partial v}{\partial Y} = 0, \tag{1}$$

$$u\frac{\partial u}{\partial X} + v\frac{\partial u}{\partial Y} = -\frac{\partial}{\partial X}\left(\frac{P}{\rho}\right) + \frac{\partial}{\partial X}\left(2\nu_T\frac{\partial u}{\partial X}\right) + \frac{\partial}{\partial Y}\left[\nu_T\left(\frac{\partial u}{\partial Y} + \frac{\partial v}{\partial X}\right)\right] + F_x + \left[\frac{\partial}{\partial Z}\left(\frac{\tau_s}{\rho}\right)\right]_{Z=H}, \tag{2}$$

$$u\frac{\partial v}{\partial X} + v\frac{\partial v}{\partial Y} = -\frac{\partial}{\partial X}\left(\frac{P}{\rho}\right) + \frac{\partial}{\partial X}\left[\nu_T\left(\frac{\partial u}{\partial Y} + \frac{\partial v}{\partial X}\right)\right] + \frac{\partial}{\partial Y}\left(2\nu_T\frac{\partial v}{\partial Y}\right) + F_y + \left[\frac{\partial}{\partial Z}\left(\frac{\tau_n}{\rho}\right)\right]_{Z=H}, \tag{3}$$

where u and v are the longitudinal and lateral surface velocities, respectively; P is the mean pressure, ν_T is the turbulent viscosity; $F_x = g\sin\theta$ and $F_y = 0{\cdot}0$ are body forces in the X- and Y-direction, respectively, g is the gravitational acceleration; θ is the average water surface slope in the longitudinal direction; Z is vertical distance from channel bed; H is the average flow depth; τ_s, τ_n are the longitudinal and lateral turbulent shear stresses, respectively; and ρ is the fluid density. The two shear stress terms evaluated at the water surface which appear in equations (2) and (3) reflect the effects of the vertical variation of the turbulent shear stresses at the free surface. These stresses are related to the surface velocities u and v, the friction factor f, the von Karman constant κ, and the bed shear velocity. Adopting the eddy viscosity concept, the longitudinal turbulent shear stresses can be written as

$$\frac{\tau_s(Z)}{\rho} = \nu_T\frac{\partial u}{\partial Z}. \tag{4}$$

Assuming the power law for the vertical variation of the longitudinal velocity, it is possible to express

$$\frac{u(Z)}{U_{\text{av}}} = \frac{1+m}{m}\left(\frac{Z}{H}\right)^{1/m}, \tag{5}$$

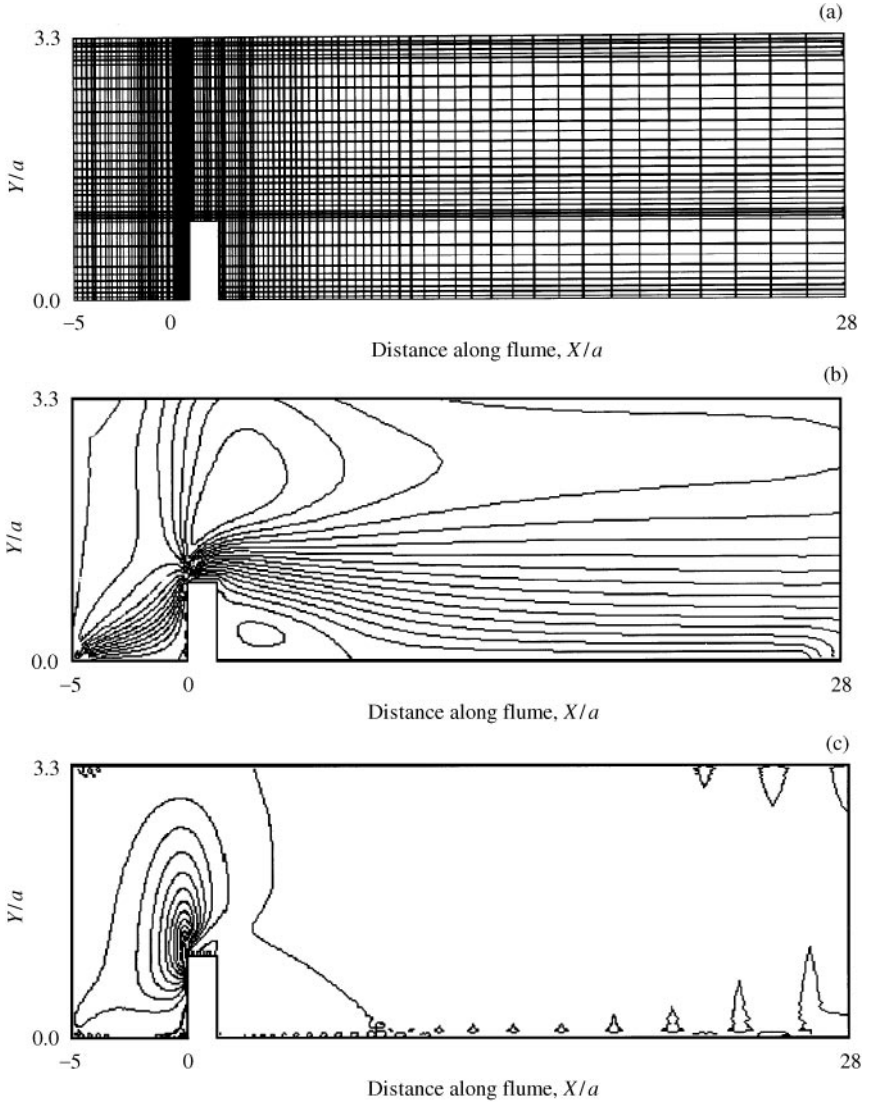

Figure 2. Finite element mesh and typical model output: (a) 4-node elements; (b) longitudinal velocity contours; (c) lateral velocity contours

where

$$m = \kappa \sqrt{\frac{8}{f}}, \tag{6}$$

in which $u(Z)$ is the longitudinal local velocity as a function of vertical distance from bed; U_{av} is the depth-averaged longitudinal velocity; and f is the Darcy-Weisbach friction factor. Assuming a parabolic distribution, an expression for the vertical variation of the turbulent viscosity can be written as

$$v_T(Z) = \kappa V_* Z\left(1 - \frac{Z}{H}\right), \tag{7}$$

in which V_* is the shear velocity ($= \sqrt{gRS_E}$); R is the hydraulic radius ($= A/P$), A being the flow area and P the wetted perimeter; S_E is the slope of the energy gradient. Substituting equations (5) through (7) into equation 4 yields

$$\left(\frac{\partial}{\partial Z}\left(\frac{\tau_s}{\rho}\right)\right)_{Z=H} = -\frac{\kappa}{H}\frac{1}{1+m}|u|\,u\sqrt{\frac{f}{8}}, \tag{8}$$

Similarly, the vertical variation of the lateral turbulent shear can be shown to be

$$\left(\frac{\partial}{\partial Z}\left(\frac{\tau_n}{\rho}\right)\right)_{Z=H} = -\frac{\kappa}{H}\frac{1}{1+m}|v|\,v\sqrt{\frac{f}{8}}. \tag{9}$$

In the derivation of equations (8) and (9), the ratio of the longitudinal shear to lateral shear stress is assumed to be equal to the square of the longitudinal velocity to lateral velocity ratio.

In the preceding formulations: (i) all quantities appearing in equations (1)–(3) are time averaged; (ii) the laminar stresses are assumed to be negligible compared to the turbulent shear stresses; (iii) the eddy-viscosity concept is applied for evaluating the turbulent stresses; and (iv) the rigid lid approximation is applied for the water surface. Assuming isotropic turbulent viscosity, the average turbulent viscosity is assumed to be the depth-average turbulent viscosity used by Laufer (1951), and Rastogi & Rodi (1978). It is given as

$$v_T = 0{\cdot}0765\, HV_*. \tag{10}$$

2.2. Numerical Solution of Governing Equations

The governing equations are solved numerically by the finite element method. In the finite element formulations, the governing equations are written in their weak form. That is, the weighted average of the governing differential equations over the domain of analysis is required to be zero for arbitrary weighting functions. Following the Galerkin method, the weighting functions are interpreted as variations in the dependent variable. In order to approximate velocity components for the two-dimensional domain of interest, the 4-node rectangular elements are used. The pressure, which is not required to be continuous over the domain, is assumed constant within each element.

Substitution of the finite element approximating functions into governing equations results in a set of integral equations. These equations are integrated over each element using four-point Gaussian quadrature. The contributions of all element integrations are added together to obtain a global matrix, the solution of which represents the finite element approximation of the boundary value problem. Due to the presence of the inertia terms, the governing equations are nonlinear; therefore the global matrix representing these terms is also nonlinear.

Due to the nonlinear nature of the governing equations, the numerical solution is obtained by assuming initial values for the variables and by iterating. The initial values assumed for the two velocity components and the pressure term were zero at all interior nodes. Gauss forward elimination and back substitution techniques are used to solve the systems of equations. After each iteration the solution vector is updated via

$$\begin{bmatrix} u \\ v \end{bmatrix}^{n+1} = \begin{bmatrix} u \\ v \end{bmatrix}^{n} + \theta \begin{bmatrix} \Delta u \\ \Delta v \end{bmatrix}^{n+1}, \tag{11}$$

where θ is the relaxation coefficient, taken as unity throughout this study, and superscripts (n) and $(n+1)$ refer to iteration counters. The iteration process is continued until the

maximum difference between two successive iterations across all the nodes of the mesh is less than a specific tolerance.

The iterative penalty approach (Zeinkiewicz 1989) is used to enforce the constraint of incompressibility. In this approach, the non-hydrostatic pressure is considered as an implicit variable adjusting itself to enforce the incompressibility constraint. The pressure is defined by

$$P^{(n+1)} = P^{(n)} - \lambda\left(\frac{\partial u}{\partial X} + \frac{\partial v}{\partial Y}\right), \tag{12}$$

where λ is the penalty parameter. Replacing the pressure term in the momentum equations, equations (2) and (3), with the definition given in equation (12) indirectly enforces the conservation of mass condition. The continuity equation, equation (1), may then be omitted from the set of governing equations, reducing the number of simultaneous equations from three to two, and therefore improving the computational efficiency. After solving the system of equations and obtaining the velocities u and v, the pressure value is updated according to equation (12).

2.3. Boundary Conditions

Boundary conditions used in the present modeling study are summarized as follows.

(i) At the upstream boundary, uniform longitudinal entrance velocities are prescribed and lateral velocities are set equal to zero ($u = U$, $v = 0$).

(ii) At the downstream boundary, for the longitudinal velocity, fully developed flow conditions (uniform flow) are applied ($\partial u/\partial X = 0$). For the lateral velocity equation, the lateral boundary shear is set to zero.

(iii) For the channel wall opposite to the abutment, virtual wall boundary conditions were applied using the logarithmic velocity distribution and smooth wall roughness conditions (Rodi 1993). The virtual boundary was located at a dimensionless distance of $Y_w = 0{\cdot}01$ B from the boundary, with the corresponding wall shear Reynolds number, $R_w\,(= Y_w V_*/v)$, of 60. This value of R_w is in agreement with the range 30 to 100 suggested by Rodi (1993).

(iv) For the wall containing the abutment, the no-slip boundary conditions ($u = 0$, $v = 0$) were applied. Along this wall, virtual wall boundary conditions at that wall are not applied since in the recirculation zone logarithmic velocity distribution is not valid.

In order to have uniform entrance and exit flow conditions, these boundaries must be sufficiently away from the abutment. Previous researchers including Thangam & Speziale (1992) and Acharya *et al.* (1993), investigating the flow over 2-D step, have pointed out that the inlet boundary should be located at least 5 times the step height upstream from the step, and that the exit section should be at least 30 step heights away from the step. These conditions were met in all of the runs: the inlet boundary was located 5 to 15 step heights upstream from the abutment while the outlet boundary was located 28 to 85 step downstream from the abutment.

2.4. Details of Finite Element Modeling

The mesh used in this study consists of 3500 elements (35 divisions across the channel width and 100 divisions along the channel length). For the modeled channel segment shown in Figure 2, a total of 3647 nodes were used. The velocity components u and v are

approximated linearly using the four-node element; while the pressure is approximated to be constant over an individual element area. As shown in Figure 2(a), the mesh is refined in the high velocity gradient zones such as around the abutment nose and near the walls. Figure 2(b, c) shows typical model output in terms of u and v contours from the nodal point velocity information.

A total of 50 iterations were found sufficient for convergence in all runs for a prescribed maximum tolerance of 10^{-6} in velocity and pressure values. The continuity constraint ($\partial u/\partial X + \partial v/\partial Y$) was also evaluated in all runs over each element; the maximum value was in the order of 10^{-11} to 10^{-14} and the minimum value was in the order of -10^{-11} to -10^{-14}. Therefore, the continuity equation was very accurately satisfied, both in the element level and on the whole flow domain (global) level.

3. MODEL VERIFICATION

In order to test and verify the computational model, a series of laboratory experiments conducted at the Colorado State University (CSU) Hydraulics Laboratory to study velocity and shear stress distribution around vertical wall abutments were used (Kheireldin 1995; Molinas, Kheireldin & Wu 1998). Additional verifications were provided through comparisons with experiments conducted to study flow around groins which can be visualized as very thin abutments (Rajaratnam & Nwachukwu 1983). In the CSU laboratory experiments, the model rectangular vertical-wall abutment structures were constructed with protrusion ratios of 0·1, 0·2, and 0·3. These experiments are characterized by their wide range of flow intensities (Froude numbers varied between 0·3 and 0·9); they complement Rajaratnam & Nwachukwu experiments in which model testing was conducted under lower flow intensities (Froude numbers varied between 0·2 and 0·3) using protrusion ratios of 0·08 and 0·16. Table 1 presents the summary of flow conditions for Kheireldin (1995) and Rajaratnam & Nwachukwu (1983) experiments along with summary of input data for the computational runs. In the model testing and verification runs, the energy slope was kept constant; only protrusion ratio and flow intensity effects were examined and compared with the experimental results.

Figures 3 through 5 present results of computations for Runs A1 through A5, B1 through B5, and C1 through C5. In these figures the lateral variation of velocities are plotted across the channel at the upstream end of the abutment ($X/a = 0$). In Figure 3(a), for a protrusion ratio of 0·1, the resultant velocities are plotted across the channel. In this figure, the lateral location, Y, is nondimensionalized by the abutment protrusion length, a, and the different profiles correspond to runs A1 through A5 results. The velocity profiles across channel are plotted again in Figure 3(b), this time by normalizing the resultant velocity, V_n, with the uniform approach velocity, V_{app}. As a result of this transformation, the series of curves in Figure 3(a) reduce to a single relationship. Finally, in Figure 3(c) the lateral variation of the turning angle is plotted. Turning angle is defined as the angle between the resultant surface velocity and the upstream approach flow. Past studies have related the turning angle to coefficient of friction and to shear stresses. At the nose region, Rajaratnam & Nwachukwu (1983) identify an upper potential flow layer and a bottom layer. They define the corresponding turning angles between the bottom streamline and the main flow direction (surface streamline) and between the main flow and the approach flow direction as α_w and α_0, respectively. The ratio between the two turning angles, $M_\alpha = \alpha_w/\alpha_0$, varies along the flow domain. The value of this ratio was found to be equal to 2 by Tingsanchali & Maheswaran (1990) using numerical experimentation. In order to account for the 3-D flow effects, Tingsanchali & Maheswaran introduced a correction for roughness according to Johnston (1960). Their corrected Chezy

TABLE 1

Summary of experimental data

Run ID	Author	Protrusion ratio a/B	Approach depth Y_{app} (m)	Centerline approach velocity V_{app} (m/s)	Friction factor f	Dimensionless velocity V_{app}/V_*	Maximum nose velocity V_n (m/s)	Measured		Computed	
								Velocity amplification V_n/V_{app}	Maximum turning angle (degrees)	Velocity amplification V_n/V_{app}	Maximum turning angle (degrees)
					Abutment experiments						
A-1	Kheireldin	0·1	0·167	0·40	0·091	9·4	0·46	1·15	–	1·17	20
A-2	Kheireldin	0·1	0·152	0·50	0·093	9·3	0·58	1·16	–	1·17	20
A-3	Kheireldin	0·1	0·143	0·59	0·094	9·2	0·68	1·15	–	1·17	20
A-4	Kheireldin	0·1	0·142	0·72	0·094	9·2	0·82	1·14	–	1·17	20
A-5	Kheireldin	0·1	0·133	0·82	0·095	9·2	0·93	1·13	–	1·17	20
B-1	Kheireldin	0·2	0·169	0·41	0·091	9·4	0·51	1·24	–	1·29	25
B-2	Kheireldin	0·2	0·147	0·49	0·093	9·3	0·62	1·27	–	1·29	25
B-3	Kheireldin	0·2	0·141	0·58	0·094	9·2	0·75	1·29	–	1·29	25
B-4	Kheireldin	0·2	0·158	0·68	0·092	9·3	0·85	1·25	–	1·29	25
B-5	Kheireldin	0·2	0·130	0·78	0·095	9·2	0·98	1·26	–	1·29	25
C-1	Kheireldin	0·3	0·147	0·25	0·093	9·3	0·38	1·52	–	1·51	29
C-2	Kheireldin	0·3	0·150	0·42	0·093	9·3	0·58	1·38	–	1·51	29
C-3	Kheireldin	0·3	0·147	0·45	0·093	9·3	0·67	1·49	–	1·51	29
C-4	Kheireldin	0·3	0·150	0·58	0·093	9·3	0·80	1·38	–	1·51	29
C-5	Kheireldin	0·3	0·163	0·73	0·092	9·3	1·08	1·48	–	1·51	29
					Groin experiments						
A1	Rajaratnam & Nwachukwu	0·167	0·189	0·25	smooth	–	0·30	1·18	20	1·20	20
A2	Rajaratnam & Nwachukwu	0·167	0·223	0·22	smooth	–	0·25	1·18	20	1·20	20
A3	Rajaratnam & Nwachukwu	0·167	0·256	0·19	smooth	–	0·22	1·18	20	1·20	20
A4	Rajaratnam & Nwachukwu	0·167	0·152	0·32	smooth	–	0·37	1·18	20	1·20	20
A5	Rajaratnam & Nwachukwu	0·167	0·152	0·24	smooth	–	0·29	1·18	20	1·20	20
B1	Rajaratnam & Nwachukwu	0·083	0·152	0·35	smooth	–	0·38	1·08	20	1·09	20
B2	Rajaratnam & Nwachukwu	0·083	0·219	0·23	smooth	–	0·25	1·08	20	1·09	20
B3	Rajaratnam & Nwachukwu	0·083	0·189	0·24	smooth	–	0·26	1·08	20	1·09	20

Notes: 1) Approach Velocity is computed in Rajaratnam & Nwachukwu experiments by dividing total discharge by flow area.
2) In Rajaratnam & Nwachukwu (1983), for each set of experiment (Set A or Set B), only an average velocity amplification value is given.
3) Maximum nose velocity is measured at the upstream end of abutment, at $X/a = 0$.

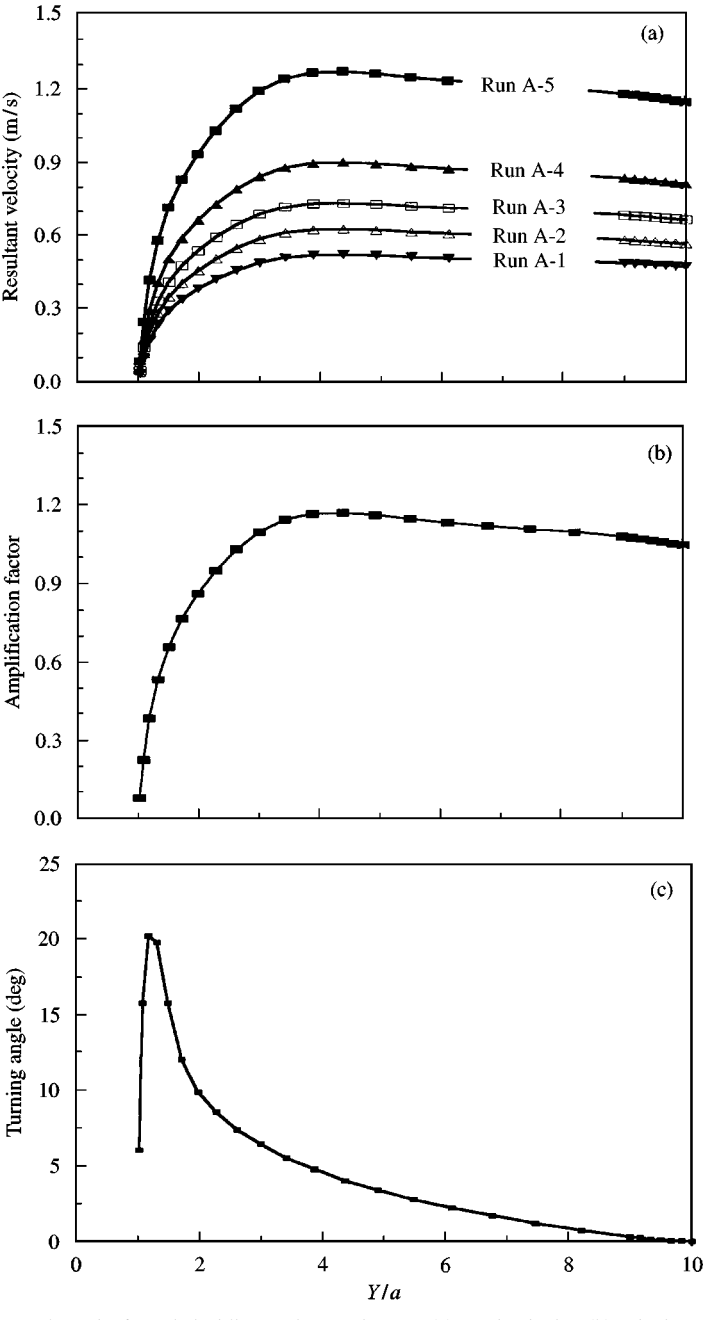

Figure 3. Compound results for Kheireldin Set A experiments: (a) total velocity, (b) velocity amplification; and (c) turning angle variations across channel at $X/a = 0$ (nose)

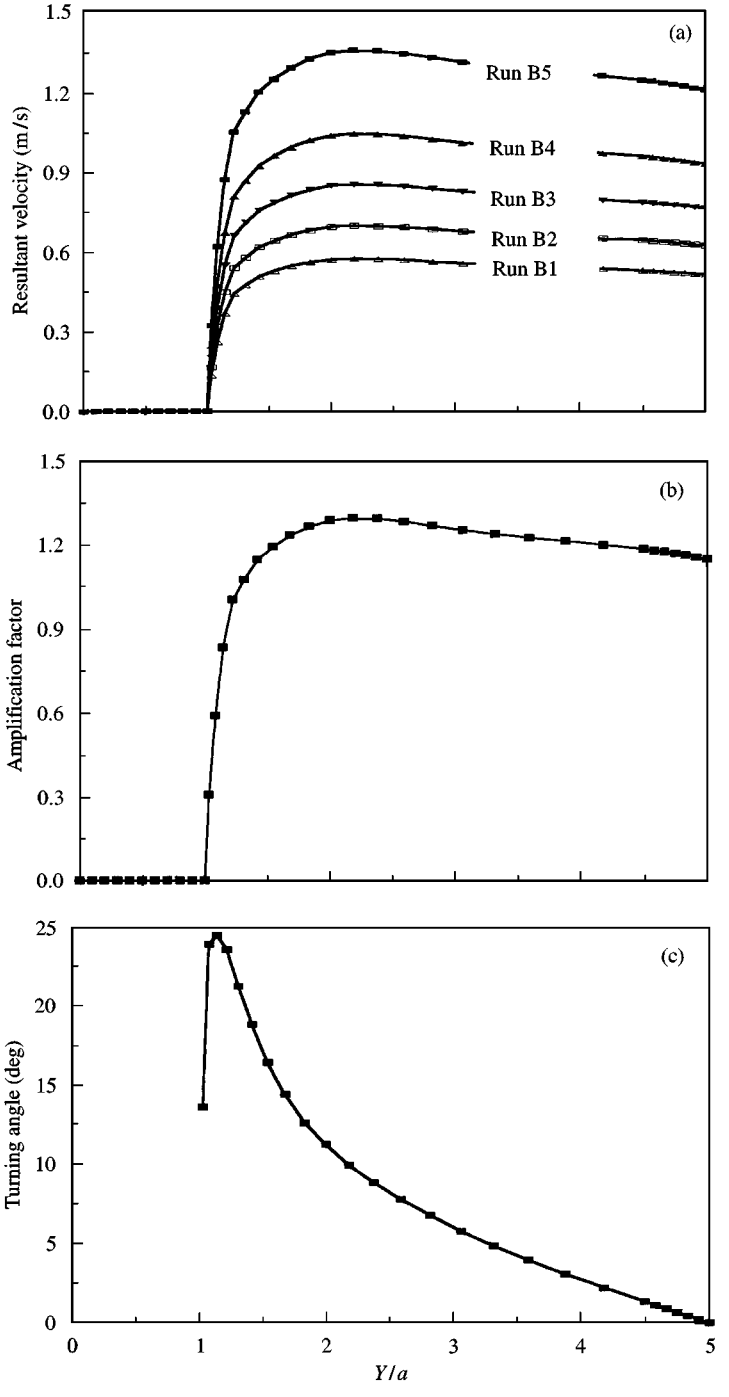

Figure 4. Computed results for Kheireldin Set B experiments: (a) total velocity; (b) velocity amplification; (c) turning angle variations across channel at $X/a = 0$ (nose)

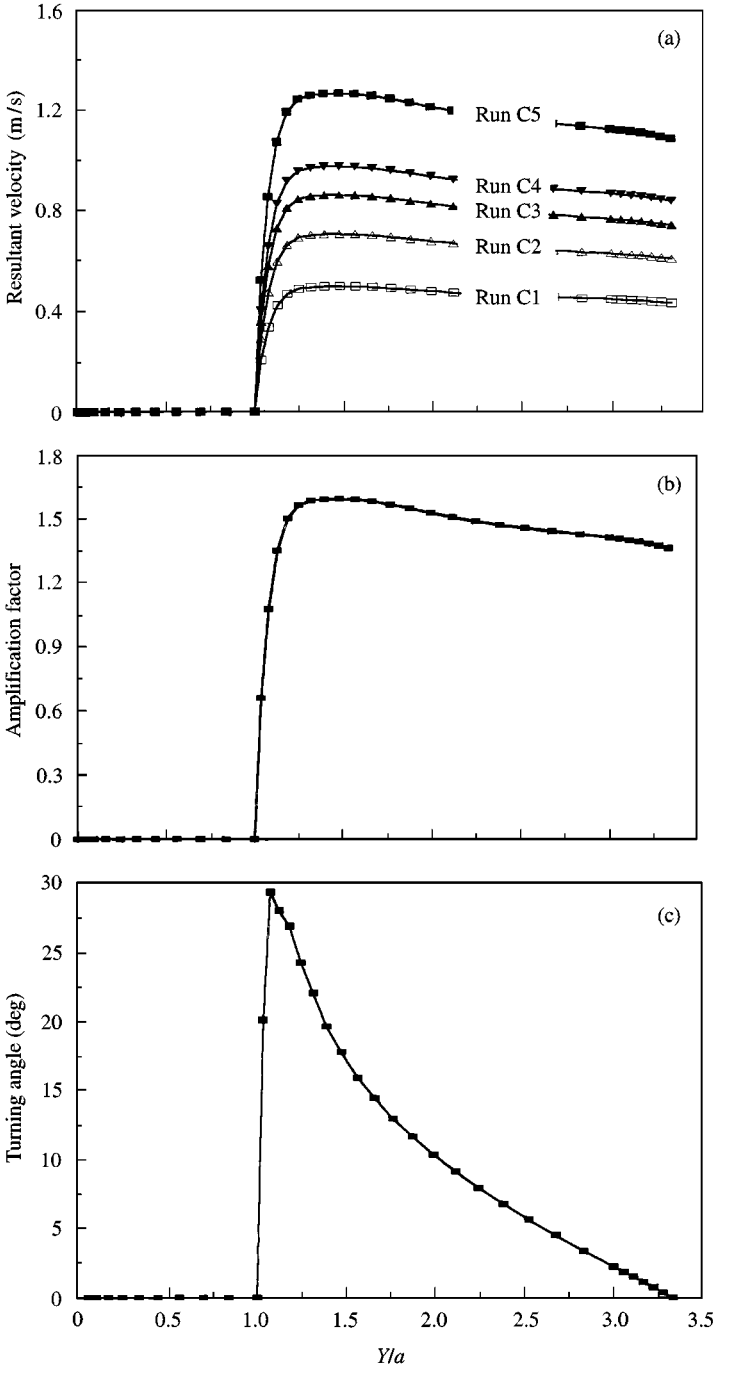

Figure 5. Computed results for Kheireldin Set C experiments: (a) total velocity; (b) velocity amplification; (c) turning angle variations across channel at $X/a = 0$ (nose)

friction coefficient, C_{fc}, is given by

$$C_{fc} = C_f \sqrt{1 + \tan^2(M_\alpha \alpha_0)}, \tag{13}$$

where C_f is the Chezy roughness coefficient ($C_f = \sqrt{8g/f}$). Using the Tingsanchali & Maheswaran approach, nose shear stresses can be computed from

$$\tau_{\text{nose}} = \rho \; C_{fc} \; V_{\text{nose}}^2, \tag{14}$$

where V_{nose} is the resultant nose velocity. As shown in Figure 3(c), the turning angle rapidly increases near the abutment boundary. It reaches its maximum value near $Y/a = 1{\cdot}2$, and decays gradually across the channel. Beyond the lateral location of $Y/a = 3$, the value of the turning angle is less than 5°, pointing out that the flow is almost parallel to the free stream and that the v component of velocity is almost zero. Figures 4(a–c) and 5(a–c) show the same behavior for protrusion ratios of 0·20 and 0·30, respectively. As shown in Figures 3 through 5, the maximum values of velocity amplification, $A_v (= V_n/V_{\text{app}})$, and the turning angle, α_0, vary with protrusion ratio. The comparison of these values with measured data are given in Table 1 and Figure 6. Since the protrusion ratios used in Rajaratnam & Nwachukwu experiments were close to the ratios used in Sets A and B computations (0·08 and 0·17 as opposed to the 0·10 and 0·20, respectively), results of groin experiments are also used in the comparisons.

Table 1 and Figure 6(a, b) show the measured and computed turning angles along the study reach using Rajaratnam & Nwachukwu (1983) data. The measurements indicate a steep gradient at the upstream abutment nose region which are in close agreement with computations. At lateral location of $Y/a = 1{\cdot}5$, the turning angle is computed to be 15° and 16° for protrusion ratios of 0·1 and 0·2 compared to the measured values of 18° for the Rajaratnam & Nwachukwu's 0·08 and 0·17 protrusion cases. For protrusion ratio of 0·1, Figure 3 shows the maximum computed turning angle to be between 18° and 20° which agrees with the measured angle. As shown in Figures 3 through 5, while the turning angle remains relatively constant at $Y/a = 1{\cdot}5$ for protrusion ratios between 0·1 and 0·3 (around 16°), at $Y/a = 1{\cdot}2$ turning angles reach their maximum values. These values range between 20° for protrusion ratio of 0·1; 27° for protrusion ratio of 0·2; and 32° for protrusion ratio of 0·3. Past the nose region, computed turning angles for vertical wall abutments vary slightly from the measured groin modeling results. This deviation is due to physical differences between abutments and groins. Abutment length along the flow direction has flow straightening effects past the nose region; whereas for groins a more pronounced recirculation zone immediately downstream from the nose region is observed.

Table 1 and Figure 6(c) show the measured and computed velocity amplifications as a function of protrusion ratios. As shown in this figure, the computed nose velocity amplifications are in close agreement with experimental measurements for a wide range of flow and protrusion ratio conditions. Rajaratnam & Nwachukwu data lie slightly below the computed amplifications since they represent slightly different roughness and depth conditions.

Figure 7 shows the computed water surface topography for a protrusion ratio of 0·3 and high approach velocity. Water surface elevation in Figure 7 shows a significant drop at the nose region whereas it is raised upstream from the protrusion. The drop at the nose region extends laterally as well as longitudinally. The lowest water surface elevation takes place downstream from the abutment nose region, close to the structure. This water surface topography is in close agreement with observed topographies (Kheireldin 1995).

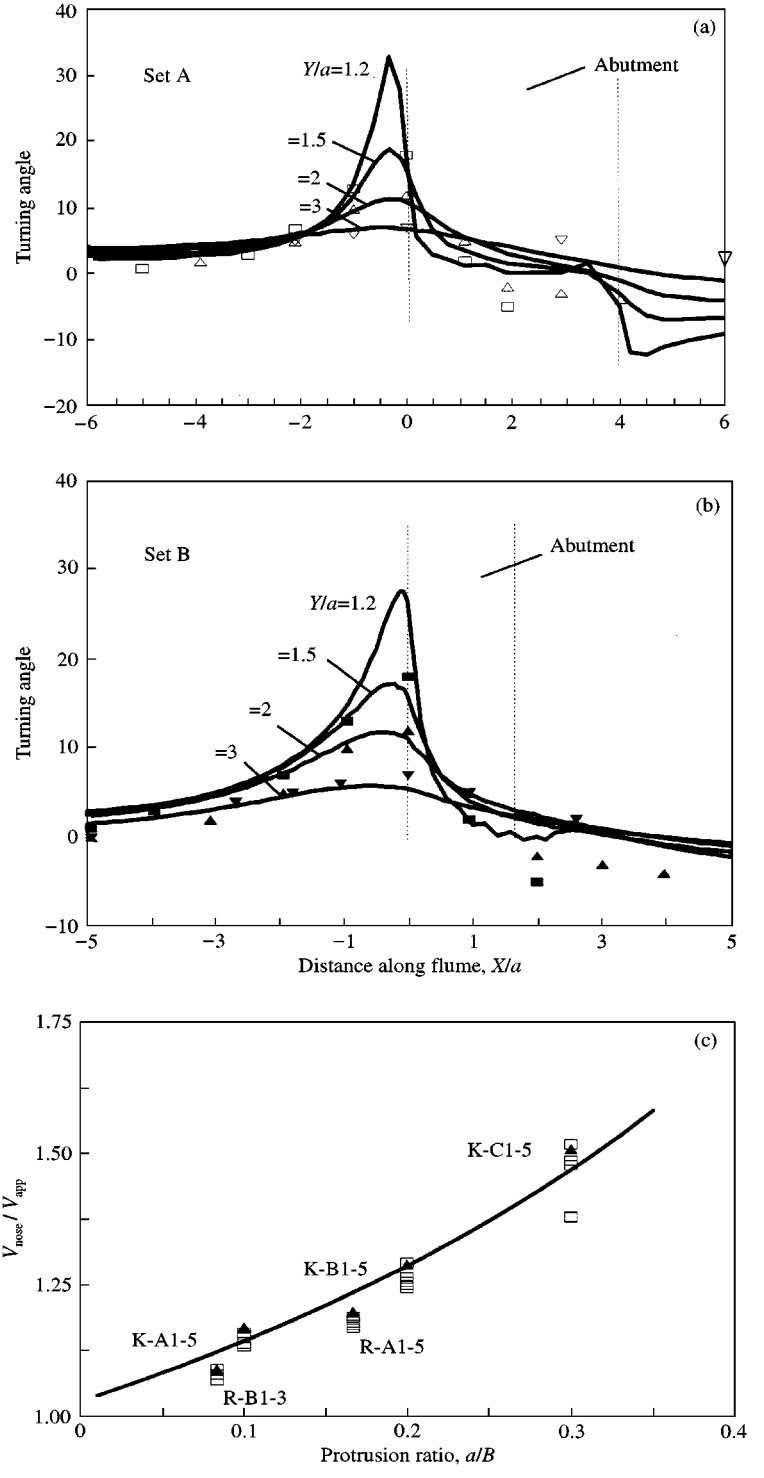

Figure 6. Comparison of computed turning angles and velocity amplifications with experimental data: (a) turning angles at $\sigma = 0{\cdot}1$; (—, computed; □, measured at $Y/a = 1{\cdot}5$; △, measured at $Y/a = 2$; ▽, measured at $Y/a = 3$. (b) turning angles at $\sigma = 0{\cdot}2$ (—, computed; ■, measured at $Y/a = 1{\cdot}5$; ▲, at $Y/a = 2$; ▼, at $Y/a = 3$; (c) velocity amplifications as a function of protrusion ratio (□, measured; ▲, computed; —, $\Lambda_v = m_0/(1 - a/B)$.

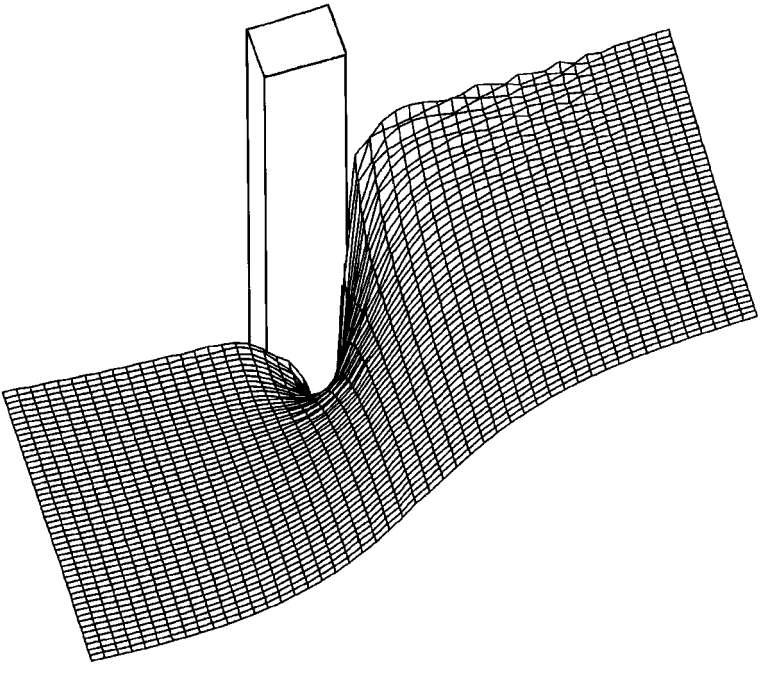

Figure 7. Computed water surface topography for 30% protrusion ratio.

4. MODEL APPLICATION

In previous laboratory studies, flow depth and channel roughness were kept relatively constant. As a result, the effect of these parameters on the velocity amplification is not known. In this phase of the study, the turbulence model was applied to investigate the flow depth and roughness effects on the velocity amplification through numerical experimentation. Table 2 presents the various test cases used in investigating roughness and flow depth effects. The test cases are grouped as: (i) constant depth and velocity runs; (ii) constant roughness runs; and (iii) constant energy slope runs.

4.1. Constant Depth and Velocity Runs

In these runs, while keeping the flow depth and velocity constant, for different protrusion ratios (0·1, 0·2, and 0·3) channel roughness is varied. Since Froude numbers corresponding to each set was kept constant, dynamic flow similarity between cases is preserved. Using dimensionless velocity ratios (V_{app}/V_*) of 40, 30, 20, and 10, series of numerical experiments were conducted. Figures 8 through 10 present results of these runs. The findings of these runs are as follows.

(i) Friction effects are felt most significantly close to the abutment structure by controlling the lateral component of the resultant nose velocity. For rough boundaries, the magnitude of lateral velocities are smaller; as channel roughness decreases, close to the abutment, the lateral velocity component and therefore the total velocity increases.

(ii) For a protrusion ratio of 0·3, for a typical range of roughness values of $f = 0{\cdot}05$ (very smooth open channel boundary) to $f = 0{\cdot}10$ (rough boundary), the increase in nose velocities due to friction factor alone was found to be up to 20%.

TABLE 2

Summary of input data to investigate depth and slope effects

Run ID	Protrusion ratio a/B	Approach depth Y_{app} (m)	Approach velocity V_{app} (m/s)	Shear velocity V_* (m/s)	Dimensionless velocity V_{app}/V_*	Friction factor f	Energy slope S_E	Froude number F_r
				Constant depth, velocity; roughness variation				
A5-R1	0·1	0·133	1·030	0·0251	40·96	0·0048	0·001	0·90
A5-R2	0·1	0·133	1·030	0·0502	20·48	0·0192	0·004	0·90
A5-R3	0·1	0·133	1·030	0·1004	10·24	0·0768	0·016	0·90
B5-R1	0·2	0·130	0·994	0·025	39·76	0·0051	0·001	0·88
B5-R2	0·2	0·130	0·994	0·050	19·88	0·0204	0·004	0·88
B5-R3	0·2	0·130	0·994	0·100	9·94	0·0816	0·016	0·88
C5-R1	0·3	0·163	0·792	0·0263	30·06	0·0089	0·001	0·62
C5-R2	0·3	0·163	0·792	0·0400	19·80	0·0204	0·00231	0·62
C5-R3	0·3	0·163	0·792	0·0800	9·90	0·0816	0·00925	0·62
				Constant slope; roughness and depth variation				
C1-R1	0·3	0·147	0·312	0·02574	12·120	0·054462	0·001	0·260
C1-R2	0·3	0·0815	0·189	0·02200	8·569	0·108940	0·001	0·211
C1-R3	0·3	0·652	0·778	0·03208	24·240	0·013616	0·001	0·308
C1-R4	0·3	0·326	0·510	0·02977	17·131	0·027260	0·001	0·285
				Constant roughness; slope and depth variation				
C1-R5	0·3	0·588	0·624	0·05148	12·120	0·054462	0·00262	0·26
C1-R6	0·3	0·0735	0·221	0·01820	12·120	0·054462	0·00073	0·26
C1-R7	0·3	0·294	0·441	0·03641	12·120	0·054462	0·00154	0·26

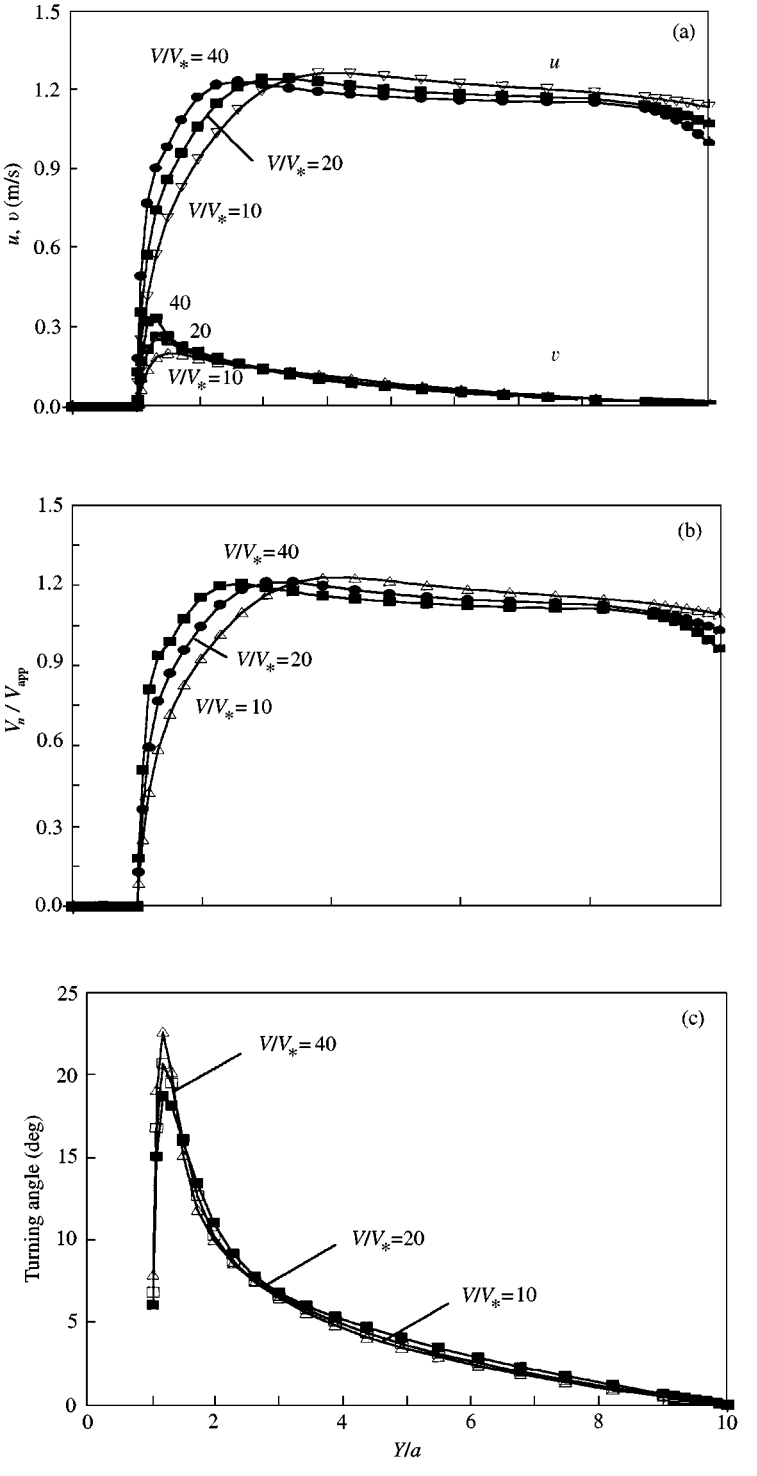

Figure 8. Effect of channel roughness for protrusion ratio of 0·1: (a) longitudinal and lateral velocity components; (b) velocity amplification; and (c) turning angle across channel at $X/a = 0$.

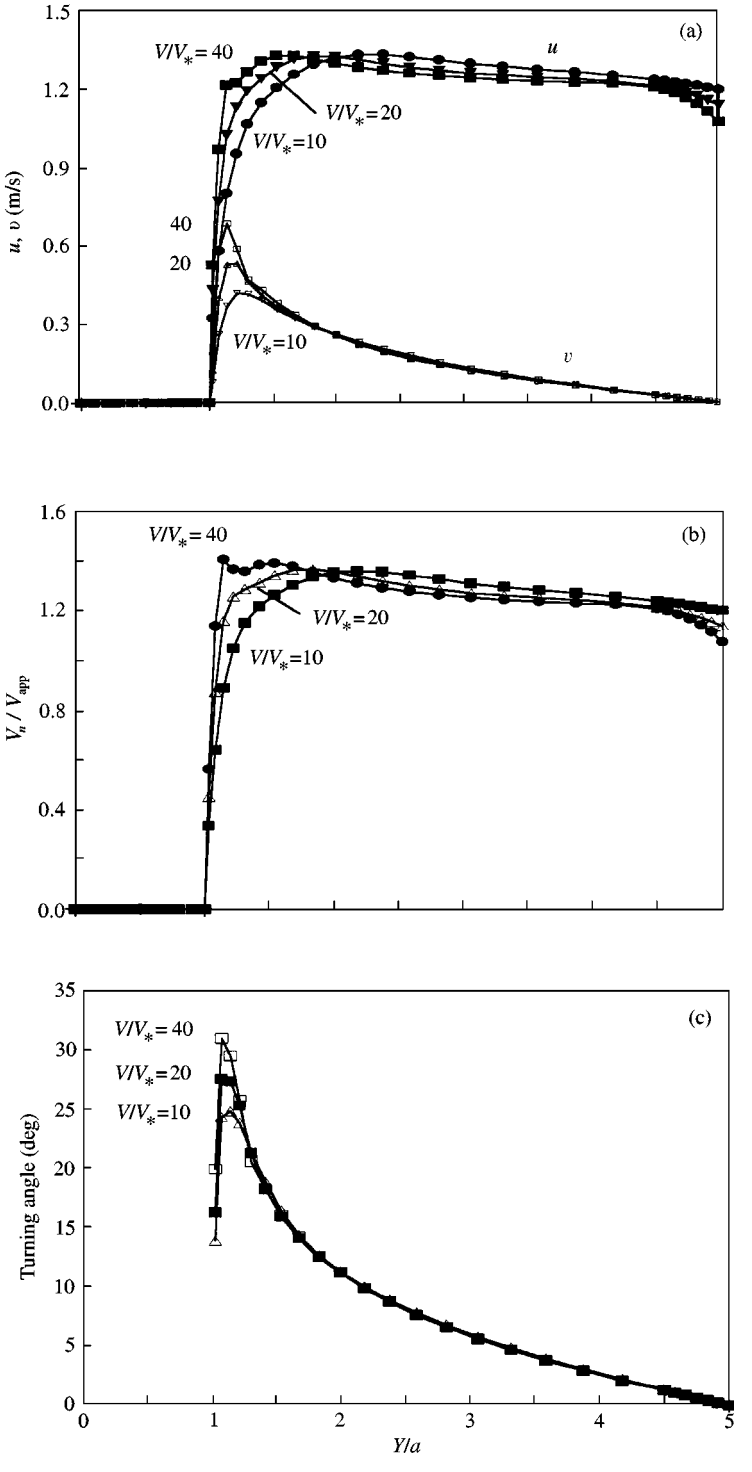

Figure 9. Effect of channel roughness for protrusion ratio of 0·2: (a) longitudinal and lateral velocity components; (b) velocity amplification; and (c) turning angle acoss channel at $X/a = 0$.

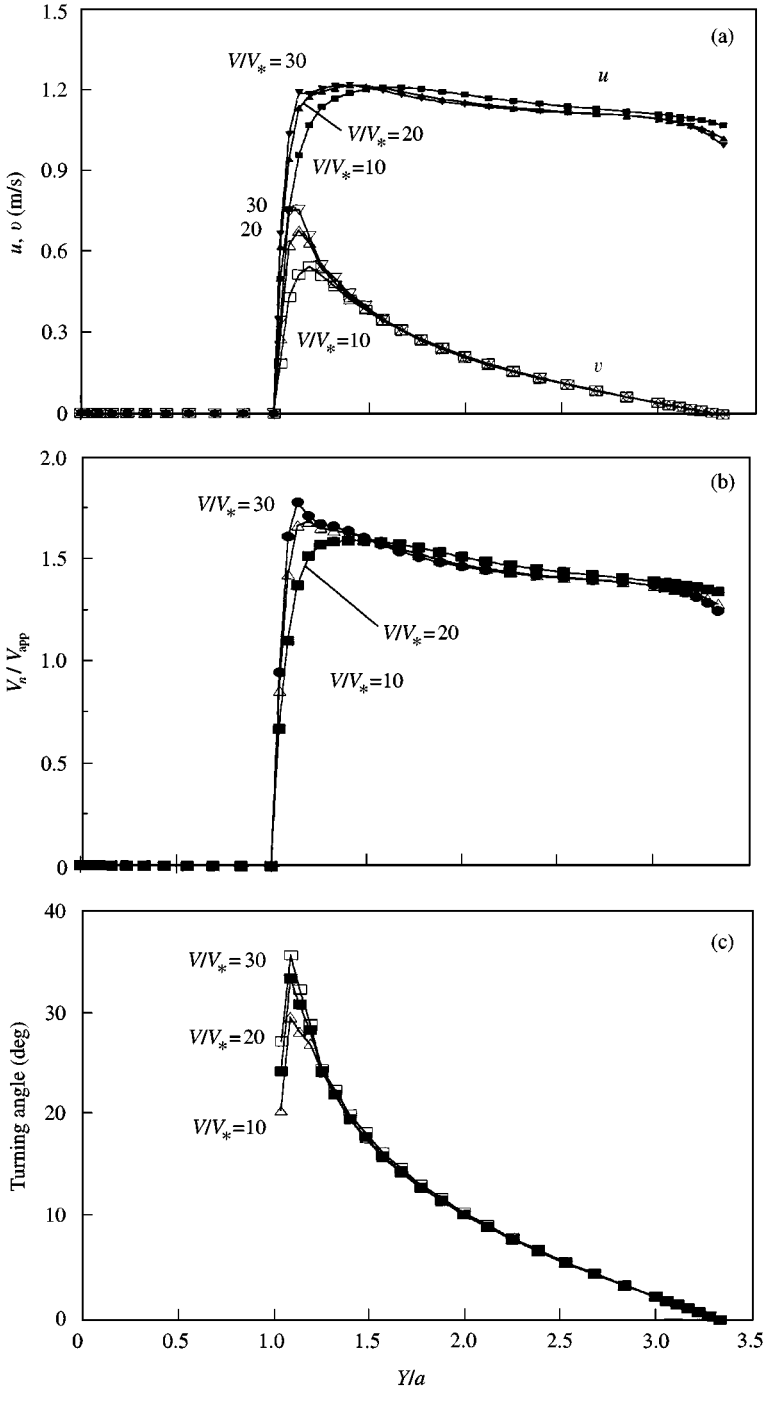

Figure 10. Effect of channel roughness for protrusion ratio of 0·3: (a) longitudinal and lateral velocity components; (b) velocity amplification; and (c) turning angle across channel at $X/a = 0$.

(iii) Amplification effects due to roughness diminishes as the protrusion ratios are reduced. For a protrusion ratio of 0·1, for the same range of roughness values ($0{\cdot}05 < f < 0{\cdot}10$), there were no significant differences in velocity amplifications. However, the location of maximum nose velocity is still shifted away from the abutment structure into the main channel.

In both Kheireldin (1995) and Rajaratnam & Nwachukwu (1983) experiments, depth and roughness were kept relatively constant. Molinas *et al.* (1998) using these data have expressed nose velocity amplification (ratio of resultant nose velocity to approach velocity), Λ_v, by

$$\Lambda_v = \frac{V_{\text{nose}}}{V_{\text{app}}} = \frac{m_0}{1-\sigma}, \tag{15}$$

where σ is the protrusion ratio ($= a/B$); and m_0 is an experimental coefficient whose value was stated to be a function of approach flow angle of attack and abutment type. For the Kheireldin experiments, Molinas *et al.* (1998) found the value of m_0 to be near 1. In the velocity amplification expression given by equation (15), the variation of m_0 with depth and roughness could not be observed. However, it is reasonable to expect that m_0, in addition to geometric factors such as flow inclination and abutment type, is also a function of channel roughness, or

$$m_0 = k_1\, F(V_{\text{app}}/V_*) = k_1\, G(f), \tag{16}$$

where k_1 is a constant and F and G are general functions of dimensionless velocity and friction factor. As a limiting condition, for small protrusion values (no protrusion), m_0 should approach 1. Using the results of numerical experimentation along with nonlinear regression and the limiting condition for $a/B = 0$, the following expression for the nose velocity amplification was developed:

$$\Lambda_v = \frac{1 + (\sigma^2 \ln f)/2}{(1-\sigma)}, \tag{17}$$

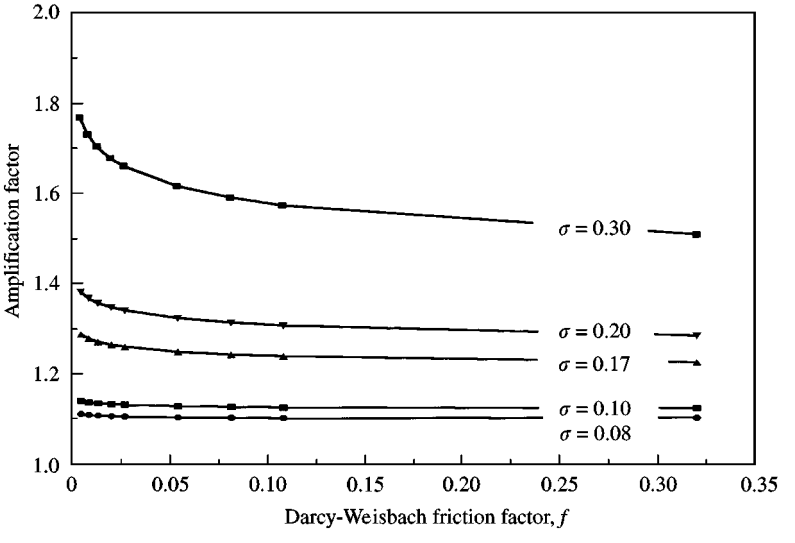

Figure 11. Variation of velocity amplification with friction factor and protrusion ratio.

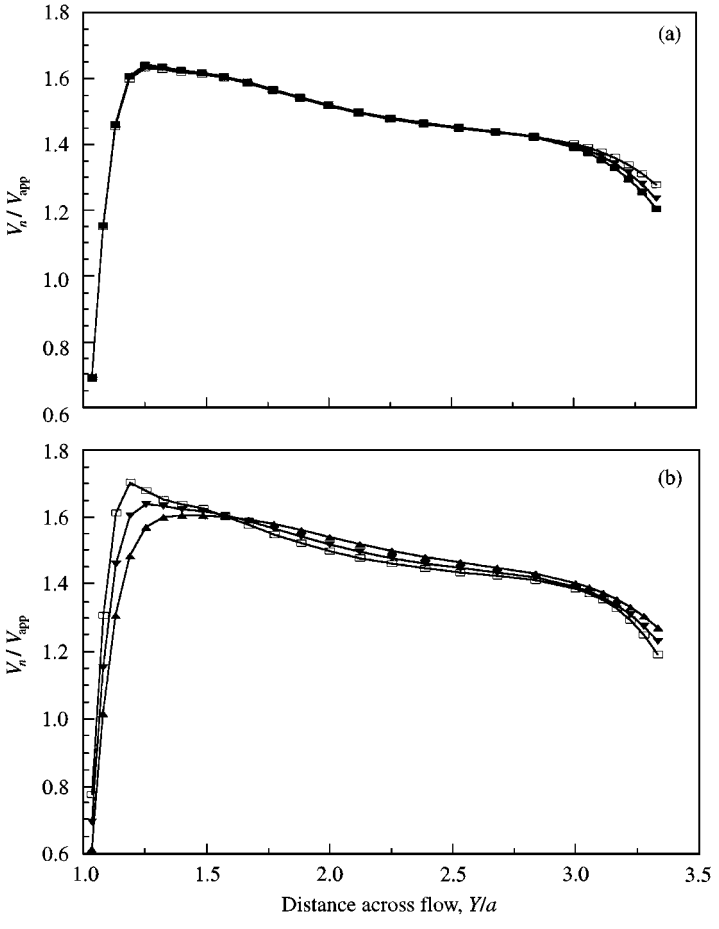

Figure 12. Results of numerical experiments: (a) effect of flow depth and energy slope for a given roughness (Froude number $F_r = 0{\cdot}26$, depth = 0·07–0·6 m, $f = 0{\cdot}0545$, $V_{app}/V_* = 12{\cdot}12$): —■—, $S = 0{\cdot}00073$; —▼—, $S = 0{\cdot}001$; —△—, $S = 0{\cdot}00154$; —□—, $S = 0{\cdot}0026$; (b) effect of roughness for a given energy slope (= 0·001) and $F_r = 0{\cdot}2$–0·3, depth = 0·08–0·65 m: —▲—, $f = 0{\cdot}108$; —▼—, $f = 0{\cdot}054$; —□—, $f = 0{\cdot}027$.

where σ is the protrusion ratio ($= a/B$) and f is Darcy-Weisbach friction coefficient. The second term which appears in the numerator in (17) reflects the friction effects. Figure 11 presents the variation of nose velocity amplification with friction factor according to equation (17). As shown in Figure 11, for friction values greater than 0·05 nose amplification is independent of channel roughness and is a function of protrusion ratio, σ, alone. On the other hand, for smooth channel boundaries (f lower than 0·05), nose amplification is a function of both σ and f. Figure 11 also shows that for protrusion ratios below 0·10, friction effects are negligible.

4.2. Constant Roughness Runs

Using a protrusion ratio of 0·3 and a constant channel roughness, approach flow depth and velocity were varied while keeping the Froude number constant. In these experiments, approach depth varied between 0·07 m and 0·59 m and velocities ranged between 0·2 m/s and 0·6 m/s. The velocity amplification profiles across the channel corresponding to different cases are given in Figure 12(a). This figure shows that for a given flow intensity (or

constant Froude number) and roughness, the velocity amplifications at the nose do not vary with depth. In other words, for a given protrusion ratio, flows with the same Froude number and friction factor result in the same nose velocity amplifications since depth effects are implicitly included in friction factors.

4.3. Constant Energy Slope Runs

In these runs, using a protrusion ratio of 0·3 and an energy slope of 0·001, flow depth and roughness were varied. Flow depths were selected between 0·08 m and 0·65 m and the corresponding friction factors ranged between 0·01 and 0·11. Similar to the results from constant depth and velocity runs, series of curves, each corresponding to a different friction factor, were obtained. The velocity amplification profiles across the channel corresponding to different cases are given in Figure 12(b) and confirms the conclusions (i) and (ii) from constant depth and velocity run experiments.

5. SUMMARY AND CONCLUSIONS

A two-dimensional hydrodynamic model was developed to determine the flow field around vertical wall abutments. The model solves the Reynolds-averaged turbulence flow equations along a horizontal plane passing through the average water surface. This approach is an improvement over the current practice of using depth-averaged models. In the model, through the use of power law for the vertical distribution of the longitudinal velocity, vertical gradient effects are accounted for. This velocity distribution is utilized in defining the vertical gradients of the longitudinal and lateral turbulent shear stress components in the momentum equations. The current model has the capability of predicting the dynamic pressure distribution, which is then converted to water surface elevations. As such, the model solves for the longitudinal velocity, lateral velocity, and local flow depth. The model being two-dimensional, is computationally efficient and practical to use. The governing equations are solved using the finite element method which is known for its ease in handling various boundary conditions and flow domain geometries.

The numerical model was successfully tested and verified against experimental data. The results show that the model could simulate the high intensity velocity and bed shear zone at the upstream abutment nose. The computed velocity amplifications at the nose region and the turning angles show close agreement with experimental measurements could be achieved for a wide range of Froude numbers ranging from 0·2 to 0·9.

Next, using this model, the effects of roughness on the flow field was investigated by varying the channel roughness while keeping other factors constant. As a result of these numerical experiments, an expression given by equation (17) which relates maximum nose velocity amplification to friction and protrusion ratio was developed. It is shown that the friction effects are felt most significantly close to the abutment structure by controlling the lateral component of the resultant nose velocity. For rough boundaries, the magnitude of lateral velocities are smaller; as channel roughness decreases, close to the abutment, the lateral velocity component and therefore the total velocity increases. For a protrusion ratio of 0·3, for a typical range of roughness values of $f = 0{\cdot}05$ (very smooth open channel boundary) to $f = 0{\cdot}10$ (rough boundary), the increase in nose velocities due to friction factor alone was found to be up to 20 percent. Amplification effects due to roughness diminishes as the protrusion ratios are reduced. For a protrusion ratio of 0·1, for the same range of roughness values ($0{\cdot}05 < f < 0{\cdot}10$), there were no significant differences in velocity amplifications. However, the location of maximum nose velocity is still shifted away from the abutment structure into the main channel. Laboratory research studies consider 8 to 10

percent protrusion ratio as a limit to study local abutment scour while avoiding contraction effects. This study finds that for this range of protrusion ratios friction effects are negligible and do not effect model-to-prototype flow similarity.

References

Acharya, S., Dutta, S., Myrum, T. A. & Baker, R. S. 1993 Turbulent flow past a surface-mounted two-dimensional rib. *ASME Journal of Fluids Engineering* **116,** 238–246.

Benque, J. P., Cunge, J. A., Feuillet, A. H. & Holly, F. M. 1982 New method for tidal current computation. *ASCE Journal of Waterway, Port, Coastal and Ocean Division* **108,** 396–417.

Bravo, H. R. & Holly, F. M. 1996 Turbulence model for depth-averaged flows in navigation installations. *ASCE Journal of Hydraulic Engineering* **122,** 718–727.

Hafez, Y. I. 1995 A k-ε turbulence model for predicting the three-dimensional velocity field and boundary shear in open and closed channels. Ph.D. Dissertation, Civil Engineering Department, Colorado State University, Fort Collins, Colorado, U.S.A.

Kheireldin, K. 1995 Shear stress and stream power distribution around vertical wall abutments. Ph.D. Dissertation, Civil Engineering Department, Colorado State University, Fort Collins, Colorado, U.S.A.

Kimura, I. & Hosoda, T. 1997 Fundamental properties of flows in open channels with dead zone. *ASCE Journal of Hydraulic Engineering* **123,** 98–107.

Laufer, J. 1951 Investigation of turbulent flow in a two-dimensional channel. Report No. 1053, NACA, Washington, D.C., U.S.A.

Mayerle, R., Toro, F. M. & Wang, S. S. Y. 1995 Verification of a three dimensional numerical model simulation of the flow in the vicinity of spur dikes. *Journal of Hydraulic Research* **33,** 243–256.

Molinas, A., Kheireldin, K. & Wu, B. 1998 Shear stress around vertical wall abutments *ASCE Journal of Hydraulic Engineering* **124,** 822–830.

Molls, T. & Chaudhry, M. H. 1995 A depth-averaged open-channel flow model. *ASCE Journal of Hydraulic Engineering* **121,** 453–465.

Ouillon, S. & Dartus, D. 1997 Three-dimensional computation of flow around groyne. *ASCE Journal of Hydraulic Engineering* **123,** 962–970.

Rajaratnam, M. & Nwachukwu, B. A. 1983 Flow near groin-like structure. *ASCE Journal of Hydraulic Engineering* **109,** 463–480.

Rastogi, A. K. & Rodi, W. 1978 Prediction of heat and mass transfer in open channels. *ASCE Journal of Hydraulics Division* **104,** 397–420.

Rodi, W. 1993 *Turbulence Models and their Application in Hydraulics. A State-of-the-Art Review*, Third Edition. Delft, Netherlands: IAHR.

Tan, W. 1992 *Shallow Water Hydrodynamics*. Elsevier Oceanography Series, 55, Amsterdam: Elsevier.

Thangam, S. & Speziale, C. G. 1992 Turbulent flow past a backward-facing step: a critical evaluation of two-equation models. *AIAA Journal* **30,** 1314–1320.

Tingsanchali, T. & Maheswaran, S. 1990 2-D Depth-averaged flow computation near groyne. *ASCE Journal of Hydraulic Engineering* **116,** 71–86.

Zienkiewicz, O. C. 1989 *The Finite Element Method*, Fourth Edition, Vol. 1. New York: McGraw-Hill.

APPENDIX: NOTATION

The following symbols are used in this paper.

a	protrusion length perpendicular to the direction of flow
B	total channel width
F_x	body force in the longitudinal channel direction
F_y	body force in the transverse channel direction
f	Darcy-Weisbach friction factor
g	gravitational acceleration
H	average water depth
k	turbulence kinetic energy
M_α	ratio between turning angles for bottom and surface streamlines, or α_w/α_0
m	reciprocal of the exponent in the power law for the longitudinal velocity
m_0	experimental coefficient in velocity amplification factor relationship
P	mean pressure

S_E slope of the energy grade line
U_{av} depth-averaged longitudinal velocity
u, v longitudinal and transverse components of local velocity, respectively
V_* shear velocity
V_n resultant nose velocity
V_{app} Width- and depth-averaged uniform longitudinal approach velocity
X longitudinal channel direction
Y transverse channel direction
Z vertical direction
α_0 turning angle between the approach flow and the main flow direction (surface streamline)
α_w turning angle between the bottom streamline and the main flow direction
ε rate of dissipation of the turbulent kinetic energy
θ angle the channel bed makes with the horizontal plane in the direction of flow
κ von Karman constant
Λ_v velocity amplification defined as the ratio of resultant nose velocity to approach velocity
λ penalty parameter
ν_T turbulent viscosity
ρ density of the water
σ ratio of protrusion length perpendicular to direction of flow to total channel width ($= a/B$)
τ_s longitudinal turbulent shear stress
τ_n transverse turbulent shear stress.